Magnetic hardness of graded interface exchange spring L10-FePt films with Co nanoinclusions

Charles Paleo, Fabrice Wilhelm, Philippe Ohresser, Edwige Otero, Andre Dias, Nora M Dempsey, Olivier Boisron, Clément Albin, Véronique Dupuis, Damien Le Roy

Magnetic hardness of graded interface exchange spring $L1_0$-FePt films with Co nanoinclusions.

Charles Paleo,[1,*] Fabrice Wilhelm,[2] Philippe Ohresser,[3] Edwige Otero,[3] Andre Dias,[4] Nora M. Dempsey,[4] Olivier Boisron,[1] Clément Albin,[1] Véronique Dupuis,[1] and Damien Le Roy[1]

[1] *Institut Lumière Matière, Université Claude Bernard Lyon 1, CNRS, F-69622, Villeurbanne, France*
[2] *The European Synchrotron Radiation Facility (ESRF), 38000 Grenoble, France*
[3] *Synchrotron SOLEIL, L'Orme des Merisiers, Saint-Aubin-BP 48, 91192 Gif-sur-Yvette, France*
[4] *Institut Néel, Université Grenoble Alpes, F-38000 Grenoble, France*

(Dated: October 15, 2021)

Hard-magnetic films with precisely tuned switching fields are of great interest for microsystems, when both the manipulation and the stability of the magnetization are brought into play. Here, we report on the exchange spring mechanism developed in compositionally-graded nanocomposite films of FePt integrating x per cent of Co nanoclusters (x varying from 0 to 50%), made from a combination of mass-selected cluster beam deposition (MS-LECBD) and e-beam evaporation. This technique offers a precise control over the nanoinclusion size (8 nm diameter) and its volume fraction in the host FePt matrix. The focus is put on the interplay between the local microstructure and the magnetic coercivity through a combinatorial approach that involves local determinations of composition, magnetization reversal from scanning magneto-optical Kerr effect and element-specific spin and orbital magnetic moments from X-ray magnetic circular dichroism. We show that Co-rich inclusions allow a fine tuning of the coercivity and that a consequent increase of effective magnetic spin moment at the Co edge is obtained in our system.

I. INTRODUCTION

Current spintronic technologies for non-volatile memory involves a recording layer with an anisotropy high enough to avoid loss due to thermal instability at room temperature. In this case, both soft ferromagnetic writing and reading head, and a high energy product spinning motor are required. The discovery of Giant Magnetoresistance (GMR) [1] allowed the transition from longitudinal to perpendicular recording, leading to higher storage densities [2], but requires an even greater anisotropy from the recording layer compared to longitudinal recording, as the anisotropy field must withstand the demagnetizing field [3].

The anisotropy energy of a magnetic grain is $E_a = K_u \times V$. As the volume V of the grain decreases, the anisotropy K_u needs to be increased to ensure magnetization stability at room temperature. However, writing becomes harder and therefore more energy-consuming [4]. To allow easier writing, one solution could be to add a softer layer on top of the stable media which serves to initiate the reversal which then propagates to the harder layer by exchanged-coupling (exchange-coupled composite, ECC) at the interface [5–7]. For this nucleation layer, oriented grains with an easy axis at 45°can be used, lowering by half the required field for reversal, according to the Stoner–Wohlfarth model [8, 9]. Graded media can also be used, softer near the writing head, the coercivity increasing with depth [3, 10]. In both cases, the minimal energy needed for the reversal is equal to that needed to create the domain wall in the hard phase [11, 12]. Studies on graded material has already been carried out on CoPt [13] and FePt [10, 14] where a decrease in coercivity of up to 60% has been observed, but highlight the need of precise characterization of both structure and magnetism.

In this context, nanocomposite benchmark systems where the microstructure should be controlled at the nanometer scale, are expected to give interesting insights. In this work, we produce FePt films integrating face-centered-cubic (fcc) Co nanoclusters (Co-NCs), using a mass selected cluster beam deposition (MS-LECBD) technique, combined with an *in-situ* electron beam evaporator. From atomic force microscopy (AFM), we verified the Gaussian-like profile of the cluster beam, as expected for MS-LECBD using laser vaporization [15]. Grown films are compositionally graded in Co-NCs, which allows us to screen the nanocomposite magnetic properties as a function of the soft inclusion concentration. Within the combinatorial approach [16, 17], several magnetic scanning probe techniques have been developed for high throughput studies, including superconducting quantum interference device (SQUID)-based microscopy [18, 19] or Hall microscopy [20, 21]. Here we used a scanning magneto-optical Kerr effect (MOKE) system with a microsecond pulsed magnetic field source capable of producing fields up to 10 T [22]. In particular, we studied the evolution of the coercive field with the volume fraction of Co-NCs and compared it with alloyed films of equivalent compositions and determined specific atomic magnetic moments as a function of the soft magnetic inclusion composition from X-ray magnetic circular dichroism (XMCD).

* charles.paleo@univ-lyon1.fr

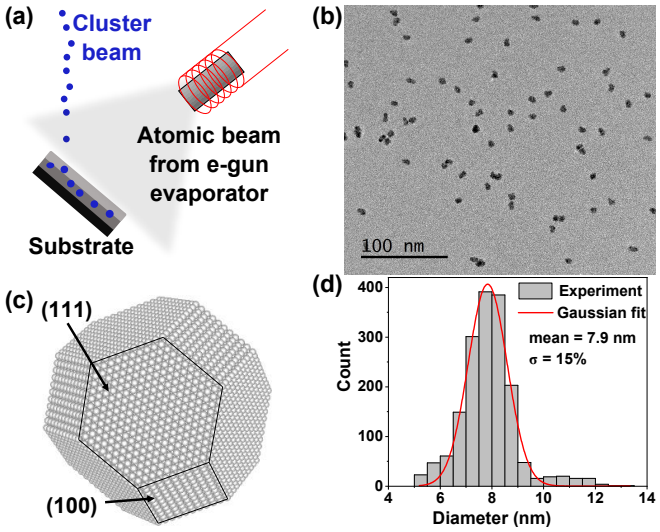

FIG. 1. **(a)** Schematic view of the sample preparation. **(b)** Transmission Electron Microscopy image of an assembly of Co nanoclusters. **(c)** schematic view of a fcc-Co truncated octahedron of the mean size [23]. **(d)** Statistical analysis of the Co nanoclusters' diameter.

II. EXPERIMENTAL METHOD

Co-NCs are produced by gas-phase condensation, in a MS-LECBD system using laser vaporization, and deposited in a soft-landing regime [24]. Our experimental set-up integrates an *in-situ* electron beam evaporator with four crucibles to embed the NCs in any hosting material. In this study, the deposition incident angles on the substrate, both for the cluster beam and the atoms from the evaporator, are of 45°(Fig. 1a).

Fig. 1b shows a transmission electron microscopy (TEM) image of the produced Co-NCs supported on an amorphous carbon membrane, and Fig. 1d the corresponding analysis of the cluster size distribution. In this work, Co-NCs are selected in mass, leading to a Gaussian size distribution centered around 7.9 nm in diameter with a 15% dispersion. In our previous work, we showed that such as-produced Co-NCs crystallize in a fcc structure, and form truncated octahedra exhibiting the co-existence of (111) and (100) facets [25], as expected from the Wulff model and represented on the schematic view of Fig. 1c.

All Co-NC depositions are made with the same settings for the clusters source and the electrostatic deviator, in order to ensure the same density profile of the cluster beam. We prepared specific samples to thoroughly calibrate the Co-NCs deposition profile by means of atomic force microscopy (AFM). Co-NCs were deposited onto on a silicon substrate with a native SiO_2 layer. Prior to deposition, Au/Ti marks for X and Y coordinates along two orthogonal directions of the plane were patterned by photolithography and lift-off techniques. AFM images of 1 μm^2 were then recorded at every millimeter along the X and Y directions. Fig. 2a shows the reconstructed cartography of the density of clusters. Note that this was repeated once again, during another run of deposition, at several weeks interval, to validate the calibration, and further confirmed by superimposing the Co X-rays Absorption Spectroscopy (XAS) signal mapping prior to Extended X-Ray Absorption Fine Structure (EXAFS) and XMCD local measurements.

The $Co_x@(FePt)_{1-x}$ nanocomposite films are deposited at room temperature in an ultra-high vacuum (UHV) chamber (base pressure of 10^{-10} mbar), on a silicon substrate with a native SiO_2 layer. They are obtained by sequential deposition of Co-NCs, and atomic bilayers of Fe (1.2 nm in thickness) and Pt (1.4 nm in thickness), repeated six times in total and subsequently annealed at 700C for 20 min in order to obtain the $L1_0$-FePt hard magnetic phase [26, 27]. Throughout the deposition area, the surface coverage of the Co-NCs in each layer is of about 21%. The clusters' flux in the deposition chamber is measured using a Faraday cage before and after each cluster layer. Due to the incidence angle of 45°, the deposition areas of the NCs' beam and the atoms from the evaporator form ellipses, with a long axis to short axis ratio of $\sqrt{2}$. The atoms from the evaporator cover a larger area of the substrate than the NCs, characterized by a long axis of 20 mm and 8 mm, respectively.

III. RESULTS AND ANALYSIS

A. Compositionally-graded Co@FePt NC films

The Co-NCs' deposition leads to the formation of an ellipse with a long axis to short axis ratio of 1.35, slightly less than $\sqrt{2}$ (Fig. 2a). The maximum density is found to be off centered within the ellipse, the concentration being nearly symmetric with respect to the major axis of the ellipse and highly asymmetric along the Y direction. As a result, considering the deposition profile along the Y axis at $X = 0$, the density gradient is about six times larger when going downward as compared to in the upward direction. Along this line, the variation of density is nearly linear (see Fig. 2b) between a maximum density of 1100 NCs/μm^2 down to 0 over a distance of 8 mm from the center.

The footprint of the Co-NCs' beam on the substrate is significantly smaller than the FePt atomic beam deposition area. Besides, the thickness and the magnetic properties of the FePt deposit, studied by AFM, X-ray reflectivity and scanning MOKE were found to be even over an area that is 6 times larger than the region containing Co nanoclusters (see Supporting Information [28] Fig. S1). Therefore, a single deposition contains a large region of homogeneous Co-free FePt film. Fig. S2 gathers the structural and magnetic properties of the FePt reference region and how the chemical ordering scales with the hard-magnetic properties of the FePt compound. The formation of the $L1_0$-FePt phase is accompanied by an increase of the coercive field, up to 1.5 T. It is worth men-

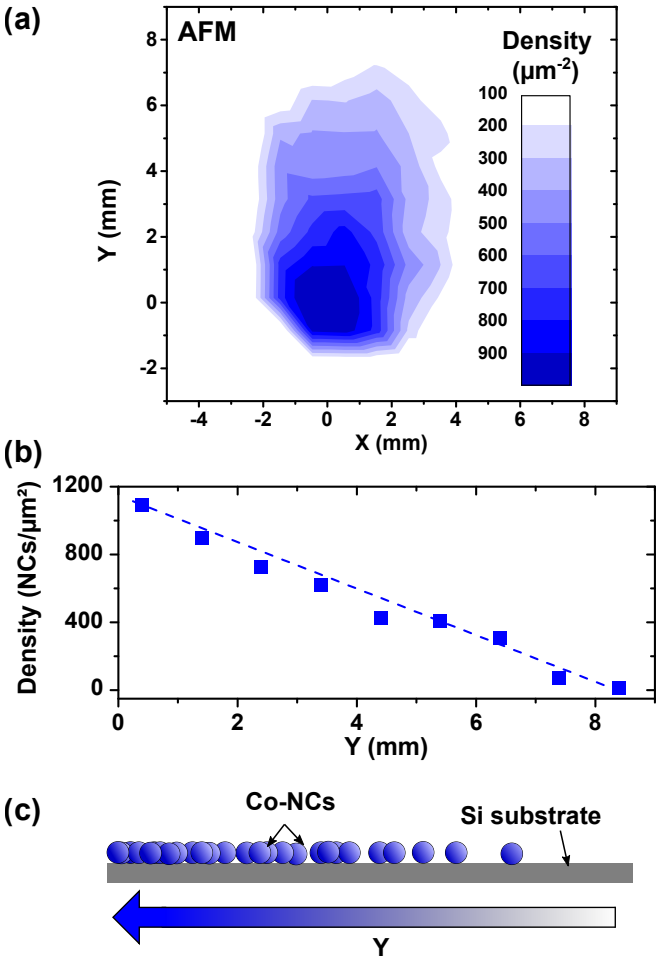

FIG. 2. Co-NCs' deposition profile. **(a)** Reconstructed map of the Co-NCs' density on a surface, from AFM observations. For this, images of area of 1×1 μm^2 were made. **(b)** Conversion of the measured AFM Co-NCs density and the Co concentration in the nanocomposite film. The blue dashed line is a linear guide to the eye. **(c)** Schematic profile of the compositionally-graded Co NCs on a Si substrate.

tioning here that tapping-AFM observations of the film's surface revealed a smooth surface of 1 nm roughness (not shown).

Based on the thoroughly calibrated deposition of the Co nanoinclusions, the deposition parameters were set to obtain a compositionally-graded $Co_x@(FePt)_{1-x}$ film with x varying from 0 to 50% (atomic proportions), over 8 mm.

B. Magnetic characterization

Local hysteresis loops were measured using a scanning polar MOKE system [22]. The system is equipped with a bipolar pulsed current source coupled with a Cu-coil of inner (outer) diameter ∼3 (10) mm. The length of individual field pulses is of the order of 16 μs, and the delay between positive and negative field pulses is about 10 ms. The hollow center of the coil allows the incident and reflected light beams to pass through. The film under measurement is scanned in-plane below the coil using an X-Y stage (minimum step size $= 2$ μm) and the coil to sample distance is set to 100 μm. Out-of-plane magnetization curves were measured every 500 μm in the X and Y directions across the film's surface. Fig. 3a shows the reconstructed map of the coercive field. The colorscale shows the value of coercive magnetic field and the variation of the coercive field matches with the footprint of the Co nanoinclusions deposition. Combining the density of deposited Co-NCs and the coercive field value leads to the average dashed curve of Fig. 3b. The symbols correspond to the results over a line at $X = 1$ and Y starting at 0, as schematized in Fig. 3c.

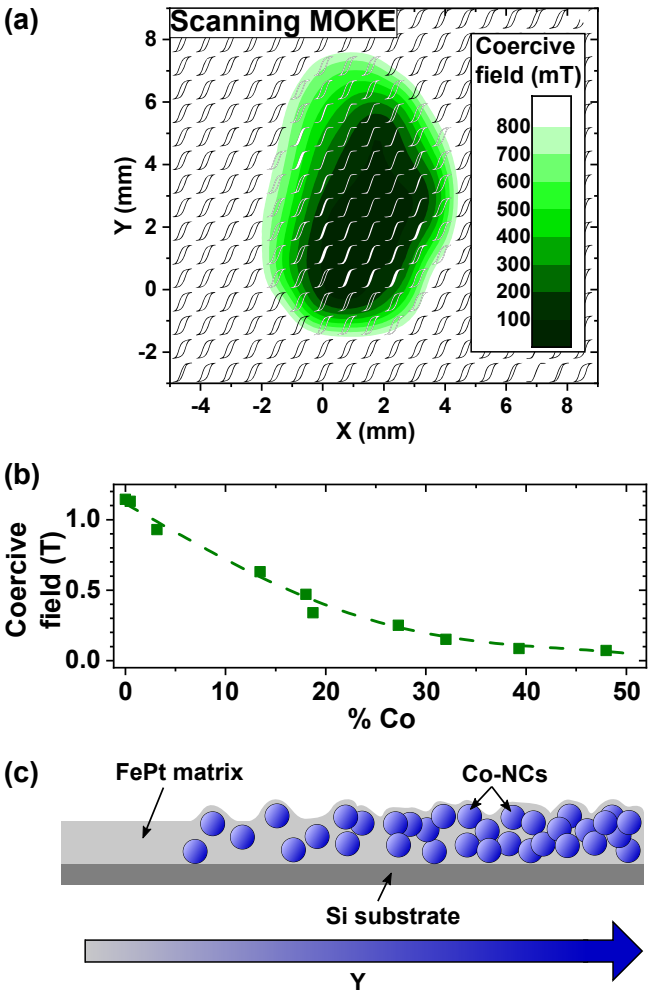

FIG. 3. **(a)** Coercive field mapping over the clusters' deposition area of the Co@FePt nanocomposite film, from scanning MOKE with measured hysteresis cycles superimposed. **(b)** Deduced compositional dependence of the nanocomposite coercive field (dashed line is a third order polynomial interpolation). **(c)** Schematic profile of the compositionally-graded $Co_x@(FePt)_{1-x}$ film, as deposited.

Moreover, scanning XMCD measurements have also been carried out (on the DEIMOS beamline at SOLEIL

synchrotron [29, 30]) in total electron yield (TEY) and fluorescence to probe element-specific magnetic properties at the $L_{2,3}$ edges of Fe and Co. The sample was scanned every 500 μm along the long axis of the Co cluster deposition area to analyze the evolution of the atomic magnetic moments with the Co content.

The magnetic moment reversal recorded at the L_3 edge of Fe and Co (Fig. 4) shows a clear single magnetic phase behavior over the whole range of Co-NCs content (0 to 50%), indicating a strong coupling between Co and Fe, in these graded-interface nanocomposite films. The decay of the coercive field with the Co content appears to be linear in XMCD while it decreases faster on SMOKE analysis (shown on Fig. 3b), probably as an effect of the probed depth: around 5 nm for XMCD TEY measurements [31, 32], 20 nm for MOKE [22]. Therefore, while MOKE probes the entire thickness of the sample, roughly a quarter of the sample is analyzed in XMCD.

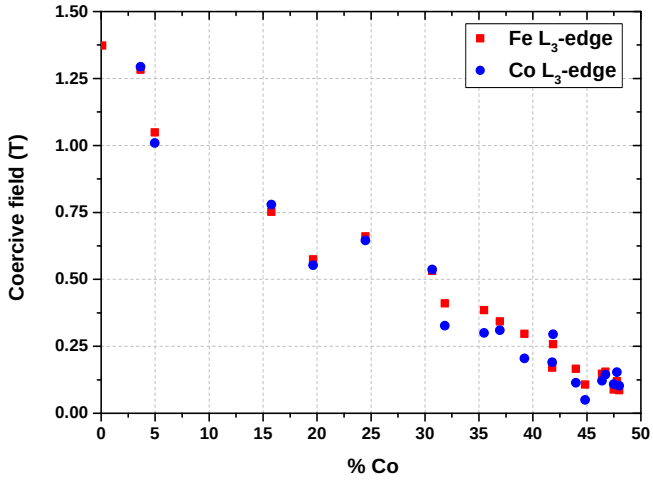

FIG. 4. Coercive field at the Fe and Co L_3-edges as a function of Co-NCs content.

XAS spectra were recorded at room temperature, under an external field of 5 T parallel to the incident X-ray beam and perpendicularly to the sample plane (90°). XMCD spectra on Fe $L_{2,3}$ peaks show a systematic increase of intensity when the Co content increases, as expected for higher amount of Co-Fe bonds (getting closer to $Fe_{65}Co_{35}$) (Fig. 5) [3].

Sum rules [33, 34] were applied to quantify the orbital and effective spin moments of Co and Fe on TEY measurements. The spectra were normalized and the continuum has been subtracted from the XAS for each polarization. The number of holes used in calculation is 3.7 for Fe (reported value for $L1_0$-FePt [35]) and 2.42 for Co (fcc bulk value calculated using the fully relativistic Dirac linear muffin-tin orbital band-structure method, [36]). The magnetic dipole term, which cannot be neglected in highly anisotropic phases such as $L1_0$-FePt here [37], has not been removed. Therefore, only the effective spin moment is being shown and compared to other effective spin moments found in the literature

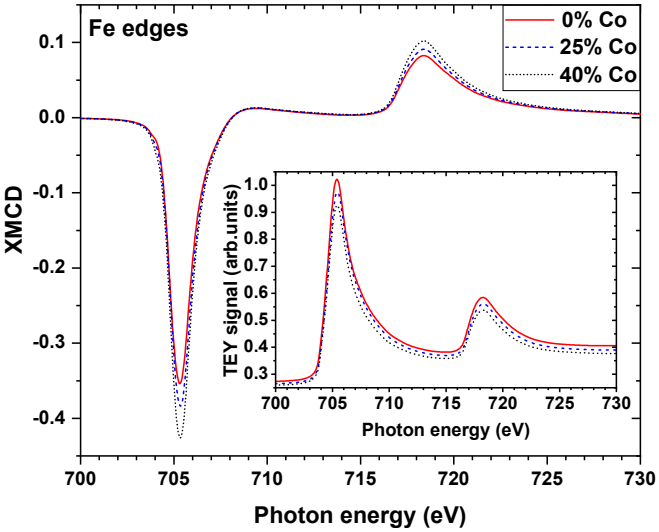

FIG. 5. TEY acquisition of the XAS and XMCD at Fe $L_{2,3}$ edges for various Co content. An increase in Co content raises the intensity of the peaks.

[35, 38–41] (denoted μ_S(Fe) and μ_S(Co) for Fe and Co, respectively). The results are displayed as a function of the Co content on Fig. 6 (Fig. S4). To our knowledge, only a few works, like Sakamoto *et al.* [37], were reported on the element-specific magnetic moments of the ternary FeCoPt alloy, shown as a comparison in Fig. S3.

The effective spin moment at Fe edges increases continuously with the Co content, from 2.35μ_B in the Co-free area up to 2.76μ_B in the Co richest area (50% Co). The absolute value reaches the higher range of reported values for chemically ordered $L1_0$-FePt, or Fe_3Pt [35]. However, the large dispersion of the absolute values found in the literature show its high sensitivity to the chemical and structural order [35, 38]. The proximity of Fe atoms to Co favors the increase of the Fe atomic moment, as predicted by the rigid band model of Slater-Pauling, and experimentally measured on B2 FeCo [42]).

The increase of the Fe spin moment is nearly linear but displays a slight change of slope at around 35% Co. In the Fe-Pt alloy, the structural transition from tetragonal $L1_0$ to face-centered-cubic $L1_2$ is expected to occur between 65% and 68% Fe, with potential intermediate A1 solid solution face-centered-cubic [43]. However, given that the orbital moment of Fe is greater in the $L1_0$ phase than in the $L1_2$ phase, one could expect that this structural change comes with a drastic decrease in the orbital moment when the Co content increases. But our findings show instead a nearly constant μ_L/μ_S ratio, suggesting a similar trend for both μ_L and μ_S. In a recent study of the chemical structure of Co@FePt nanocomposite films studied by EXAFS [27], analysis showed that Co-rich regions are well described by fcc $(Co+Fe)_3Pt$ chemical environment.

As opposed to μ_S(Fe), μ_S(Co) decreases linearly when

the Co content increases. Interestingly, the slope is similar to the one that goes from the μ_S(Co) measured in CoPt [35, 38, 41] to the one in Co (hcp) [32, 39] (slope better viewed on Fig. S5). This is in good agreement with the persistence of Co-rich regions after annealing that are larger when the Co content increases. The absolute value of μ_S(Co) is systematically higher (ranging from 1.99μ_B at high Co content to 2.08 μ_B at lower concentration) as compared to 1.98μ_B in disordered CoPt [38] or 1.62μ_B in bulk hcp Co [32, 39]. However, the high values of μ_S(Co) must be taken with caution as the number of holes in NCs often differs from the one of the bulk [44, 45]. Moreover, surface-induced anisotropy in clusters can sometimes lead to either a lift [46] or a reinforcement [47] of the orbital moment quenching typically found in 3*d* transition-metals, depending on the cluster size and interaction with the matrix.

Contrary to μ_L(Fe) which increases, we found that μ_L(Co) remains nearly constant, at 0.21μ_B, over the whole range of concentration. Like in Fe-Pt alloy, it is established that the proximity effect of Co and Pt on the Co magnetic moment highly depends on the structure. An increase in magnetic moment is expected for distorted FeCo alloys [48]. In our samples, the tetragonal $L1_0$ matrix could have induced a distortion of the Co-rich inclusion. The experimental work of Ueno *et al.* on ultra-thin Co layers sandwiched in between Pt layers showed that as the fraction of Co-Pt bonds with respect to Co-Co increases, the spin and orbital moments decrease while the ratio μ_L/μ_S is constant [49]. In contrast, density functional theory-generalized gradient approximation (DFT-GGA) computations on small CoPt alloyed clusters by Hu *et al.* [50] revealed a systematic increase of the Co magnetic moment as the number of Co-Pt bonds increases.

The ratio μ_L/μ_S at both Fe and Co edges does not vary with the overall composition, showing a similar variation of μ_S and μ_L for each element. Its absolute value does not depend on the number of holes [33, 34], and remains in between the $L1_0$ phase and the $L1_2$ phase for Fe, which could suggest a mixture of the two structures. As for Co, the ratio μ_L/μ_S is in the high range of reported values in Co-Pt alloy. The high value of μ_L could be of structural origin in the graded interface between the Co inclusions and the matrix.

Samples were probed at two different angles, at 90° (the X-ray beam is perpendicular to the sample plane, and the electric field lies in the plane of the sample) and at 30°(with thus a non-zero out-of-plane component of the electric field). The results are summarized in Table I for Fe and Table II for Co, in order to investigate the magnetocrystalline anisotropy [52, 53].

At the Fe edges, μ_L is systematically larger in the plane of the sample. This is even stronger in the regions that contain Co. At the Co edges, in contrast, μ_L is slightly

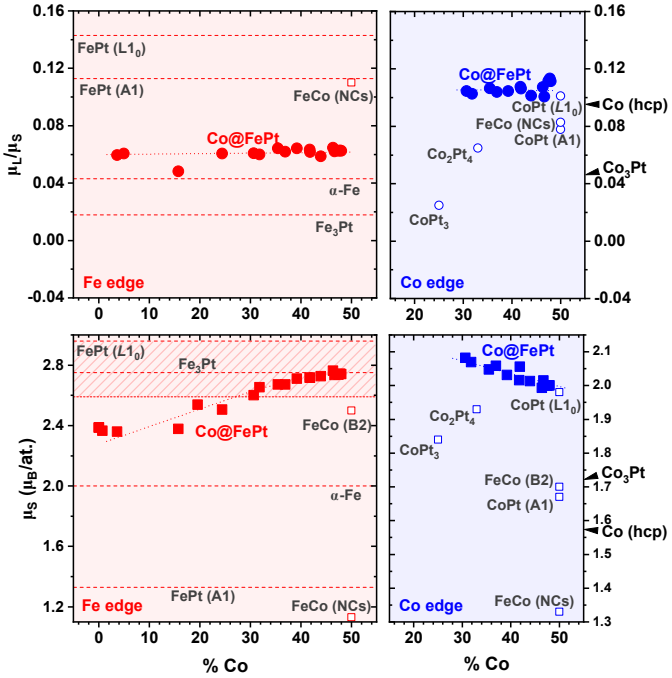

FIG. 6. Orbital/spin moment ratio and spin moment as a function of Co content for various materials (from [35, 38–42, 51]) along with our Co@FePt samples. All references are bulk values, except when "clusters" is specified.

TABLE I. Orbital, spin moment and ratio of Fe atoms at different Co content at 90° (X-ray beam perpendicular to the sample plane) and 30°. Moments in μ_B/at.

(Fe edges) Co %	μ_L (30°)	μ_L (90°)	μ_S (30°)	μ_S (90°)	μ_L/μ_S (30°)	μ_L/μ_S (90°)
0	0.05	0.13	2.52	2.36	0.020	0.055
25	0.12	0.15	2.59	2.51	0.046	0.060
50	0.12	0.17	2.74	2.74	0.044	0.067

TABLE II. Orbital, spin moment and ratio of Co atoms at different Co content at 90°and 30°. Moments in μ_B/at.

(Co edges) Co %	μ_L (30°)	μ_L (90°)	μ_S (30°)	μ_S (90°)	μ_L/μ_S (30°)	μ_L/μ_S (90°)
25	0.23	0.21	2.31	2.08	0.10	0.10
50	0.25	0.22	2.13	2.00	0.12	0.11

smaller in-plane, as it increases by around 10% when the electric field is at 30°out of the plane. Note that as-deposited Co nanoclusters are face-centered cubic and are randomly oriented. Our findings would translate in a film plane that is easy for μ_L(Fe) but hard for μ_L(Co).

However, several effects qualify this conclusion about the anisotropy of the orbital moment. Indeed, spin-orbit coupling and interface roughness between hetero-atoms may lead to an in-plane spin reorientation, overshadowing the magnetocrystalline anisotropy. In particular, it has been shown that the presence of intermixing may

lead to the orbital anisotropy not being proportional to magnetocrystalline anisotropy [54, 55]. Besides, it is now well established that TEY measurements suffer from saturation effect which results in a recorded signal not proportional to the cross-section, especially at grazing incidence, and this effect is more pronounced for Fe than for Co atoms [31].

IV. CONCLUSION

To conclude, compositionnally-graded Co_x@$FePt_{1-x}$ nanocomposite films (x varying from 0 to 50%) were prepared by co-deposition from two independent MS-LECBD and e-beam evaporation techniques. We used combined local characterization techniques to thoroughly analyze the dependence of the magnetic properties on the concentration of Co nanoinclusions. Interestingly, the decay of coercivity is found to be substantially smaller in the nanocomposite films as compared to the alloyed configuration, as expected in a two-phase exchange spring magnet. Fe and Co magnetic moments were quantified using XMCD for the first time in such compositionnally-graded Co_x@$FePt_{1-x}$ nanocomposite films, which showed significant variations over the studied range of composition. Fe spin and orbital moments are found to increase with the Co content. Oppositely, Co spin and orbital moments, which remain relatively high as compared to any references, decrease. These unprecedented experimental findings could be of great interest for the design of semi-hard nanocomposite films with a fine tune of magnetization reversal.

ACKNOWLEDGMENTS

This work is supported by the ANR through the collaborative project SHAMAN (ANR-16-CE09-0019), and the doctoral school ED PHAST. The authors thanks Rémy Fulcrand and Agnès Piednoir, from the ILM laboratory for fruitful discussion and technical support in the cleanroom and AFM experiments. XAS and XMCD experiments were performed on the DEIMOS beamline at SOLEIL Synchrotron, France. We are grateful to the SOLEIL staff for smoothly running the facility.

[1] M. N. Baibich, J. M. Broto, A. Fert, F. N. Van Dau, F. Petroff, P. Etienne, G. Creuzet, A. Friederich, and J. Chazelas, Giant magnetoresistance of (001)fe/(001)cr magnetic superlattices, Physical Review Letters **61**, 2472–2475 (1988).

[2] U. Hartmann, *Magnetic Multilayers and Giant Magnetoresistance: Fundamentals and Industrial Applications* (Springer Berlin Heidelberg, 2000).

[3] J. M. D. Coey, *Magnetism and Magnetic Materials*, 1st ed. (Cambridge University Press, 2001).

[4] M. M. Vopson, E. Zemaityte, M. Spreitzer, and E. Namvar, Multiferroic composites for magnetic data storage beyond the super-paramagnetic limit, Journal of Applied Physics **116**, 113910 (2014).

[5] R. Victora and X. Shen, Composite media for perpendicular magnetic recording, IEEE Transactions on Magnetics **41**, 537 (2005).

[6] J. Chen, L. Huang, J. Hu, G. Ju, and G. Chow, Fept–c graded media for ultra-high density magnetic recording, Journal of Physics D: Applied Physics **43**, 185001 (2010).

[7] R. Skomski, T. A. George, and D. J. Sellmyer, Nucleation and wall motion in graded media, Journal of Applied Physics **103**, 07F531 (2008).

[8] K.-Z. Gao and H. N. Bertram, Magnetic recording configuration for densities beyond 1 tb/in 2 and data rates beyond 1 gb/s, IEEE transactions on magnetics **38**, 3675 (2002).

[9] C. Varvaro, *Ultrahigh-density magnetic recording: storage materials and media designs* (Pan Stanford Publishing, 2016).

[10] D. Goll, A. Breitling, L. Gu, P. A. van Aken, and W. Sigle, Experimental realization of graded l10-fept/fe composite media with perpendicular magnetization, Journal of Applied Physics **104**, 083903 (2008).

[11] D. Suess, Multilayer exchange spring media for magnetic recording, Applied Physics Letters **89**, 113105 (2006).

[12] A. Goncharov, T. Schrefl, G. Hrkac, J. Dean, S. Bance, D. Suess, O. Ertl, F. Dorfbauer, and J. Fidler, Recording simulations on graded media for area densities of up to 1tbit/in.2, Applied Physics Letters **91**, 222502 (2007).

[13] K. Mitsuzuka, T. Shimatsu, H. Muraoka, H. Aoi, N. Kikuchi, and O. Kitakami, Magnetic properties of co–pt/ co hard/soft stacked dot arrays, Journal of Applied Physics **103**, 07C504 (2008).

[14] H. Wang, H. Zhao, T. Rahman, Y. Isowaki, Y. Kamata, T. Maeda, H. Hieda, A. Kikitsu, and J.-P. Wang, Fabrication and characterization of fept exchange coupled composite and graded bit patterned media, IEEE transactions on magnetics **49**, 707 (2013).

[15] R. Alayan, L. Arnaud, A. Bourgey, M. Broyer, E. Cottancin, J. R. Huntzinger, J. Lermé, J. L. Vialle, M. Pellarin, and G. Guiraud, Application of a static quadrupole deviator to the deposition of size-selected cluster ions from a laser vaporization source, Review of Scientific Instruments **75**, 2461–2470 (2004).

[16] M. L. Green, I. Takeuchi, and J. R. Hattrick-Simpers, Applications of high throughput (combinatorial) methodologies to electronic, magnetic, optical, and energy-related materials, Journal of Applied Physics **113**, 9_1 (2013).

[17] A. J. Zambano, H. Oguchi, I. Takeuchi, Y. Choi, J. S. Jiang, J. P. Liu, S. E. Lofland, D. Josell, and L. A. Bendersky, Dependence of exchange coupling interaction on micromagnetic constants in hard/soft magnetic bilayer systems, Physical Review B **75**, 144429 (2007).

[18] A. Finkler, D. Vasyukov, Y. Segev, L. Neeman, Y. Anahory, Y. Myasoedov, M. Rappaport, M. Huber, J. Martin, A. Yacoby, *et al.*, Nano-sized squid-on-tip for scan-

ning probe microscopy, in *Journal of Physics: Conference Series*, Vol. 400 (IOP Publishing, 2012) p. 052004.
[19] Y. Shperber, N. Vardi, E. Persky, S. Wissberg, M. E. Huber, and B. Kalisky, Scanning squid microscopy in a cryogen-free cooler, Review of Scientific Instruments **90**, 053702 (2019).
[20] D. Le Roy, G. Shaw, R. Haettel, K. Hasselbach, F. Dumas-Bouchiat, D. Givord, and N. M. Dempsey, Fabrication and characterization of polymer membranes with integrated arrays of high performance micro-magnets, Materials Today Communications **6**, 50 (2016).
[21] A. Oral, S. Bending, and M. Henini, Real-time scanning hall probe microscopy, Applied physics letters **69**, 1324 (1996).
[22] A. Dias, G. Gomez, D. Givord, M. Bonfim, and N. M. Dempsey, Preparation and characterisation of compositionally graded smco films, AIP Advances **7**, 056227 (2017).
[23] K. Momma and F. Izumi, Vesta 3 for three-dimensional visualization of crystal, volumetric and morphology data, Journal of applied crystallography **44**, 1272 (2011).
[24] V. Dupuis, G. Khadra, A. Hillion, A. Tamion, J. Tuaillon-Combes, L. Bardotti, and F. Tournus, Intrinsic magnetic properties of bimetallic nanoparticles elaborated by cluster beam deposition, Physical Chemistry Chemical Physics **17**, 27996–28004 (2015).
[25] M. Jamet, W. Wernsdorfer, C. Thirion, D. Mailly, V. Dupuis, P. Mélinon, and A. Pérez, Magnetic anisotropy of a single cobalt nanocluster, Physical Review Letters **86**, 4676–4679 (2001).
[26] H. Zeng, M. L. Yan, N. Powers, and D. J. Sellmyer, Orientation-controlled nonepitaxial l10 copt and fept films, Applied Physics Letters **80**, 2350–2352 (2002).
[27] C. Paleo, Interplay between local structure and magnetic properties of graded exchange-coupled co@fept nanocomposite films, PHYSICAL REVIEW B , 7 (2020).
[28] See supplemental material at [url] for additional figures and tables.
[29] P. Ohresser, E. Otero, F. Choueikani, K. Chen, S. Stanescu, F. Deschamps, T. Moreno, F. Polack, B. Lagarde, F. Marteau, and et al., Deimos: A beamline dedicated to dichroism measurements in the 350–2500 ev energy range, Rev. Sci. Instrum. , 9 (2014).
[30] L. Joly, E. Otero, F. Choueikani, F. Marteau, L. Chapuis, and P. Ohresser, Fast continuous energy scan with dynamic coupling of the monochromator and undulator at the deimos beamline, Journal of Synchrotron Radiation **21**, 502–506 (2014).
[31] R. Nakajima, J. Stöhr, and Y. U. Idzerda, Electron-yield saturation effects in l -edge x-ray magnetic circular dichroism spectra of fe, co, and ni, Physical Review B **59**, 6421–6429 (1999).
[32] C. T. Chen, Y. U. Idzerda, H.-J. Lin, N. V. Smith, G. Meigs, E. Chaban, G. H. Ho, E. Pellegrin, and F. Sette, Experimental confirmation of the x-ray magnetic circular dichroism sum rules for iron and cobalt, Physical Review Letters **75**, 152–155 (1995).
[33] B. T. Thole, P. Carra, F. Sette, and G. van der Laan, X-ray circular dichroism as a probe of orbital magnetization, Physical Review Letters **68**, 1943–1946 (1992).
[34] P. Carra, B. T. Thole, M. Altarelli, and X. Wang, X-ray circular dichroism and local magnetic fields, Physical Review Letters **70**, 694–697 (1993).
[35] I. Galanakis, M. Alouani, and H. Dreyssé, Calculated magnetic properties of low-dimensional systems: the aucu- and aucu3-type ferromagnets, Journal of Magnetism and Magnetic Materials **242–245**, 27–32 (2002).
[36] A. Perlov, A. Yaresko, and V. Antonov, Py-lmto, a spin-polarized relativistic linear muffin-tin orbitals package for electronic structure calculations, PY-LMTO, A Spin-polarized Relativistic Linear Muffin-tin Orbitals Package for Electronic Structure Calculations", unpublished (1995).
[37] S. Sakamoto, K. Srinivasan, R. Zhang, O. Krupin, K. Ikeda, G. Shibata, Y. Nonaka, Z. Chi, M. Sakamaki, K. Amemiya, and et al., Effects of cobalt substitution in l 1 0 -(fe,co)pt thin films, Physical Review B **96**, 144437 (2017).
[38] V. Dupuis, G. Khadra, S. Linas, A. Hillion, L. Gragnaniello, A. Tamion, J. Tuaillon-Combes, L. Bardotti, F. Tournus, E. Otero, and et al., Magnetic moments in chemically ordered mass-selected copt and fept clusters, Journal of Magnetism and Magnetic Materials **383**, 73–77 (2015).
[39] *Landolt-Börnstein Zahlenwerte und Funktionen aus Naturwissenschaften und Technik: Neue Serie: = Numerical data and functional relationships in science and technology: new series. Gruppe 3 Bd. 19 Teilbd. a: Kristall- und Festkörperphysik = Crystal and solid state physics Magnetische Eigenschaften von Metallen = Magnetic properties of metals 3d-, 4d- und 5d-Elemente, Legierungen und Verbindungen* (Springer, 1986).
[40] *Metallic Alloys: Experimental and Theoretical Perspectives* (Springer Netherlands, 1994).
[41] O. Šipr, J. Minár, S. Mankovsky, and H. Ebert, Influence of composition, many-body effects, spin-orbit coupling, and disorder on magnetism of co-pt solid-state systems, Physical Review B **78**, 12 (2008).
[42] J. M. MacLaren, T. C. Schulthess, W. H. Butler, R. Sutton, and M. McHenry, Electronic structure, exchange interactions, and curie temperature of feco, Journal of Applied Physics **85**, 4833–4835 (1999).
[43] C. J. Smithells, W. F. Gale, and T. C. Totemeier, *Smithells metals reference book*, 8th ed. (Elsevier Butterworth-Heinemann, 2004).
[44] H. Basch, M. D. Newton, and J. W. Moskowitz, The electronic structure of small nickel atom clusters, The Journal of Chemical Physics **73**, 4492–4510 (1980).
[45] F. Luis, F. Bartolomé, F. Petroff, J. Bartolomé, L. M. García, C. Deranlot, H. Jaffrès, M. J. Martínez, P. Bencok, F. Wilhelm, and et al., Tuning the magnetic anisotropy of co nanoparticles by metal capping, Europhysics Letters (EPL) **76**, 142–148 (2006).
[46] D. A. Eastham, P. M. Denby, A. Harrison, I. W. Kirkman, and A. G. Whittaker, Enhanced magnetocrystalline anisotropy in deposited cobalt clusters, Journal of Physics: Condensed Matter **14**, 605–612 (2002).
[47] D. A. Eastham, Y. Qiang, T. H. Maddock, J. Kraft, J.-P. Schille, G. S. Thompson, and H. Haberland, Quenching of ferromagnetism in cobalt clusters embedded in copper, Journal of Physics: Condensed Matter **9**, L497–L502 (1997).
[48] T. Burkert, L. Nordström, O. Eriksson, and O. Heinonen, Giant magnetic anisotropy in tetragonal feco alloys, Physical Review Letters **93**, 027203 (2004).
[49] T. Ueno, J. Sinha, N. Inami, Y. Takeichi, S. Mitani, K. Ono, and M. Hayashi, Enhanced orbital magnetic mo-

ments in magnetic heterostructures with interface perpendicular magnetic anisotropy, Scientific Reports **5**, 14858 (2015).

[50] W. Hu, H. Yuan, H. Chen, G. Wang, and G. Zhang, Structural and magnetic properties of copt clusters, Physics Letters A **378**, 198 (2014).

[51] G. Khadra, *Magnetic and structural properties of size-selected FeCo nanoparticle assemblies*, Theses, Université Claude Bernard - Lyon 1 (2015).

[52] P. Bruno, Tight-binding approach to the orbital magnetic moment and magnetocrystalline anisotropy of transition-metal monolayers, Physical Review B **39**, 865–868 (1989).

[53] J. Stöhr, Exploring the microscopic origin of magnetic anisotropies with x-ray magnetic circular dichroism (xmcd) spectroscopy, Journal of Magnetism and Magnetic Materials **200**, 470–497 (1999).

[54] P. Bruno and J. P. Renard, Magnetic surface anisotropy of transition metal ultrathin films, Applied Physics A Solids and Surfaces **49**, 499–506 (1989).

[55] C. Andersson, B. Sanyal, O. Eriksson, L. Nordstrom, O. Karis, D. Arvanitis, T. Konishi, E. Holub-Krappe, and J. H. Dunn, Influence of ligand states on the relationship between orbital moment and magnetocrystalline anisotropy, PHYSICAL REVIEW LETTERS , 4 (2007).